https://doi.org/10.5194/egusphere-2025-6481
Preprint. Discussion started: 5 January 2026

A Robust Aerosol Impact on Clouds Along the Subtropical to Tropical Transition

Netta Yeheskel[1], Matthew W. Christensen[2], Fabian Hoffmann[3], Graham Feingold[4], and Guy Dagan[1]

[1]Fredy and Nadine Herrmann Institute of Earth Sciences, Hebrew University of Jerusalem, Jerusalem, Israel
[2]Pacific Northwest National Laboratory, Richland, WA, USA
[3]Institut für Meteorologie, Freie Universität Berlin, Berlin, Germany
[4]NOAA Chemical Sciences Laboratory, Boulder, CO, USA

Correspondence: Guy Dagan (guy.dagan@mail.huji.ac.il)

Abstract. Marine clouds undergo a transition from subtropical stratocumulus (Sc) to shallow cumulus (Cu) and eventually to deep convective (DC) systems as air masses progress from the subtropics towards the deep tropics. How aerosols modulate this Lagrangian cloud evolution remains largely uncertain. Using both 5-year long satellite observations mapped along 8-day Lagrangian trajectories and complementary large-eddy simulations from nine initiation locations across the Northeast Pacific, Southeast Pacific, and Southeast Atlantic. This framework allows us to quantify the aerosol effect and its co-variability with meteorological conditions on cloud microphysics, macrophysics, and top-of-atmosphere radiation through the full Sc-Cu-DC transition. This research reveals that increasing aerosol concentrations leads to deeper, and more reflective clouds throughout this cloud transition. Examining the thermodynamic evolution along the trajectory indicates a well-known trend: enhanced moistening near the boundary-layer top and lower free troposphere in polluted cases, suggesting that some of the co-variability between aerosol and meteorological conditions is internally driven. The agreement between model simulations and satellite data alongside the multi-basin coherence of the results indicates that aerosols systematically amplify cloud depth and reflectivity during the subtropical–to–tropical cloud transition.

1 Introduction

The large-scale atmospheric overturning circulation in the tropics is a key driver of the global climate, governing the redistribution of heat, moisture, and energy across latitudes (Emanuel et al., 1994). This circulation, manifested through systems like the Hadley and Walker cells, creates regions of mean ascent and descent, which shapes patterns of tropical convection and subsidence (Bony et al., 2015). Clouds are not merely embedded within this circulation; they are strongly coupled to it. A large fraction of this cloud-circulation coupling arises from latent heating released during condensation and freezing, which directly modifies atmospheric stability and circulation strength (Neggers et al., 2007). Specifically, deep convective clouds develop in regions of rising motion, while low-level stratiform clouds form under subsiding branches of the large-scale circulation (Bony et al., 2015). The latent heating profile associated with each cloud regime modulates large-scale circulation (Neggers et al., 2007; Dagan and Chemke, 2016; Dagan et al., 2023). In addition, clouds reflect incoming shortwave solar radiation and emit longwave radiation to space (Loeb et al., 2018), processes through which they regulate Earth's radiative energy budget. It has

https://doi.org/10.5194/egusphere-2025-6481
Preprint. Discussion started: 5 January 2026

been suggested that changes in cloud macrophysical and radiative properties influence the strength and structure of the circulation itself, creating a feedback loop that links cloud formation, atmospheric dynamics, and energy balance (Voigt and Shaw, 2015; Voigt et al., 2021; Dagan et al., 2023).

Embedded within these large-scale tropical circulations is a systematic progression of cloud regimes, here referred to as the tropical cloud transition (Bony et al., 2015). As near-surface air parcels move from the cooler surface, subsiding subtropics into the warmer tropics, driven by trade winds, they encounter changing meteorological conditions that support a cloud transition from stratocumulus (Sc) decks to shallow cumulus (Cu) and eventually to deep convective clouds (DC) (Bony et al., 2015). Sc decks, which dominate the eastern basins of subtropical oceans, strongly affect the global energy budget due to their high albedo and wide spatial coverage (Wood, 2012). This tropical cloud transition is shaped by rising sea surface temperatures (SSTs) and changes in boundary layer structure along the trade winds from the subtropics towards the deep tropics, along with the pattern of ascent and descent within the Hadley cell (Wood, 2012; Myers and Norris, 2013).

Anthropogenic aerosols alter the microphysical and macrophysical properties of clouds via processes referred to as aerosol–cloud interactions (ACI) (Bellouin et al., 2020). Increases in aerosol concentrations, acting as cloud condensation nuclei (CCN), result in smaller and more numerous droplets, thus increasing the clouds' reflectivity — a process known as the Twomey effect (Twomey, 1977). The increased cloud droplet number concentration (N_d) under polluted conditions can also lead to cloud adjustments, such as the suppression of warm-rain formation, resulting in longer-lived clouds with modified vertical structure (Albrecht, 1989). These microphysical changes may further influence entrainment and mixing processes at the cloud top. Specifically, smaller cloud droplets evaporate more rapidly when mixed with dry air from the lower free troposphere, generating an evaporation–entrainment feedback that can thin or dissipate the cloud layer (Wang et al., 2003; Ackerman et al., 2004). In parallel, a reduction in droplet size may introduce a sedimentation–entrainment feedback: reduced sedimentation velocities enhance cloud-top evaporation, promoting additional entrainment of warm, dry air into the cloud (Bretherton et al., 2007). These opposing effects contribute to uncertainty in the overall aerosol impact on clouds and their evolution along the tropical cloud transition. In addition, these ACI mechanisms have been shown to depend on the cloud regime and evolve over time (Gryspeerdt et al., 2014; Dagan et al., 2017; Glassmeier et al., 2021). The effects of ACI on cloud properties are especially pronounced in low-level marine clouds such as Sc. These clouds are highly sensitive to aerosol perturbations, strongly coupled with the boundary layer, and span large portions of Earth's surface, making them key regulators of shortwave radiation (Wood, 2012; Bellouin et al., 2020; Wood, 2021; Wall et al., 2022).

Beyond the local impacts on radiation and precipitation discussed above, growing evidence suggests that aerosols can influence the evolution of cloud regimes in a broader sense (Goren et al., 2019; Christensen et al., 2020; Dagan et al., 2023). Recent studies show that the influence of ACI extends beyond changes in individual cloud properties, as it can drive changes in the transitions between different cloud regimes (Christensen et al., 2020; Goren et al., 2022) and reshape cloud evolution and development (Dagan et al., 2023). Microphysical changes such as enhanced entrainment, deepening of cloud layers, and increased mid-tropospheric humidity can feed back onto convective development and even propagate through large-scale atmospheric circulation, manifesting in far-reaching consequences for the climate system by impacting precipitation patterns and the energy budget (Abbott and Cronin, 2021; Dagan et al., 2023). These effects have been documented in both satellite observations

https://doi.org/10.5194/egusphere-2025-6481
Preprint. Discussion started: 5 January 2026

(Gryspeerdt and Stier, 2012; Christensen et al., 2016; Quaas et al., 2024) and idealized modeling studies (Dagan and Stier, 2020; Abbott and Cronin, 2021; Dagan, 2022; Dagan et al., 2023), reinforcing the need to view ACI in the context of full cloud evolution rather than isolated cloud types. By adopting a Lagrangian 'temporal' perspective in this paper, we gain insights into the dynamic evolution of cloud systems over time, allowing us to better understand the interconnected atmospheric processes that shape and transform cloud regimes. This shift in approach provides a more holistic view of cloud–aerosol–meteorology interactions and their broader implications for the climate system.

While previous work has focused primarily on ACI impacts during the Sc-to-Cu transition (Yamaguchi et al., 2015; van der Dussen et al., 2016; Goren et al., 2019; Christensen et al., 2020; Chun et al., 2025), fewer studies have examined how aerosols influence the full progression of tropical cloud regimes—including the emergence of deep convective clouds—and their associated radiative consequences (Dagan et al., 2023). In this study, we address this gap by investigating how ACI modulates tropical cloud transition across all stages using a Lagrangian perspective (Yamaguchi et al., 2017; Goren et al., 2019; Sandu et al., 2010; Yamaguchi et al., 2015; Christensen et al., 2020; Kazil et al., 2021; Erfani et al., 2025). Using satellite observations and Lagrangian cloud-resolving model simulations, we assess the influence of aerosols on the development and radiative impacts of tropical cloud systems, with the goal of improving our understanding of their role in modulating large-scale circulation and climate.

2 Methods

2.1 Satellite Data and Calculation of Lagrangian Trajectories

This research integrates four observational datasets. The Modern-Era Retrospective analysis for Research and Applications, Version 2 (MERRA-2; Gelaro et al. (2017)) provides gridded fields at 0.5° resolution with 72 vertical levels and 3-hourly temporal sampling. The Clouds and the Earth's Radiant Energy System CERES SYN1deg-1Hour Edition 4.1 product (CERES; Doelling et al. (2016)) provides gridded radiative fluxes and cloud properties at a 1° spatial and hourly resolution. These fields are derived from retrievals across 16 geostationary satellites, calibrated against Moderate Resolution Imaging Spectroradiometer (MODIS; Levy et al. (2013)) collection 5.1, and adjusted for radiative budget consistency using the Fu–Liou algorithm, with noted seasonal and diurnal biases (Hinkelman and Marchand, 2020). Comparisons with MODIS collection 6 are used to evaluate aerosol optical thickness and cloud properties, precipitation is provided by the Integrated Multi-satellitE Retrievals for GPM precipitation on a half-hourly basis on a 0.1° grid (IMERG; Huffman et al. (2020)). These datasets are collocated with the pre-calculated Lagrangian trajectories to investigate the cloud evolution, provide collocated satellite and reanalysis data, which are averaged over a 1° by 1° grid-box, and provided hourly along the trajectory. Specifically, CERES and IMERG provide geolocation data (latitude, longitude, altitude, land fraction) and collocated satellite fields, while meteorological variables are obtained from MERRA-2 and MODIS.

https://doi.org/10.5194/egusphere-2025-6481
Preprint. Discussion started: 5 January 2026

2.1.1 Lagrangian Trajectories

Lagrangian trajectories are calculated using the Hybrid Single Particle Lagrangian Integrated Trajectory model (HYSPLIT; Stein et al. (2015b)), initiated within the planetary boundary layer (PBL). In this study, HYSPLIT is driven by meteorological fields from MERRA-2. To ensure that trajectories follow the mean motions of the PBL, they are initialized in the middle of the PBL (determined by the thermodynamic sounding) and are constrained to flow along an isobaric surface to avoid escaping into the free troposphere. The depth of the PBL is calculated within HYSPLIT using profiles of temperature, humidity, and wind velocity (Stein et al., 2015a). This methodology closely follows the approach presented in Christensen et al. (2023).

2.1.2 Trajectory setup

Forward trajectories are initialized daily at 18:00 local time to approximately align with multisensor observations from the A-Train satellite constellation. Each trajectory runs for 8 days (192 hours), which is sufficient in most cases to capture the evolution of Sc-Cu-Dc as trajectories move from the subtropics toward the tropics. The dataset covers the years 2015–2019 and includes daily trajectories from nine different initiation locations for three oceanic basins: the Northeast Pacific (NEP1-3), the Southeast Pacific (SEP1-3), and the Southeast Atlantic (SEA1-3) with three initiation points in each region (see Fig. 1). Each location, therefore, consists of 1825 daily initiated trajectories. These locations span a range of different longitudes and latitudes within each basin and are all situated along the eastern boundary of the subtropical oceans, where Sc clouds are prevalent.

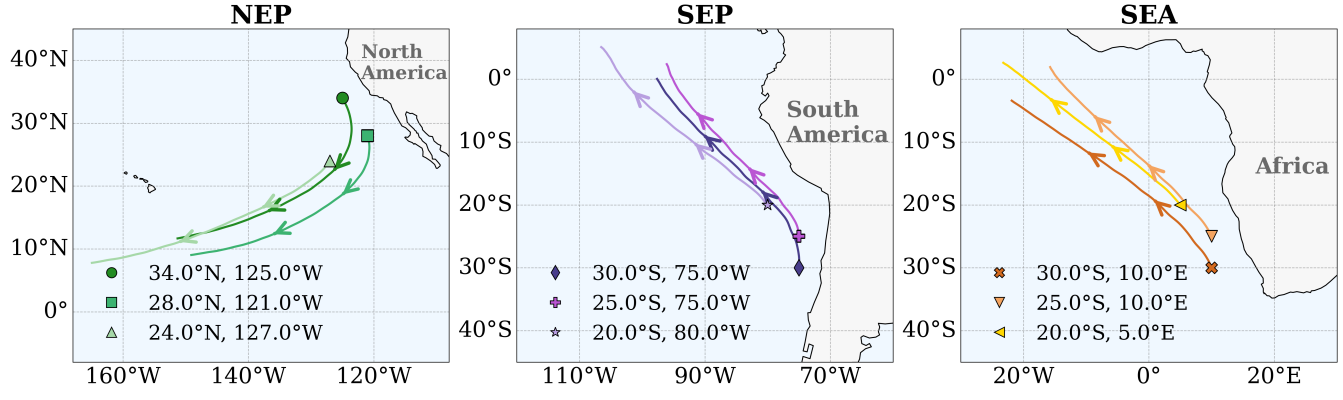

Figure 1. Mean trajectory paths across the three ocean basins: (a) Northeast Pacific (NEP), (b) Southeast Pacific (SEP), and (c) Southeast Atlantic (SEA). Each colored line represents the average trajectory path initiated from a distinct starting point, marked by a unique symbol, with arrows indicating the direction of propagation with the trade winds.

The starting points are located along the eastern coasts of subtropical oceans, where easterly winds are found on average. Thus, trajectories initialized at these points are expected to flow predominantly westward and equatorward, toward the deep tropics. To ensure a robust analysis of cloud transitions, we apply a series of constraints to filter out trajectories that do not

https://doi.org/10.5194/egusphere-2025-6481
Preprint. Discussion started: 5 January 2026

meet physical and meteorological criteria expected of the relevant cloud transition. This filtering method is critical to isolating trajectories that are representative of the tropical cloud transition and to avoid trajectories that cross over land, where the air mass would be affected by the continent.

2.1.3 Data Filtering

First, to ensure that trajectories remain representative of oceanic conditions, we apply a land fraction threshold of less than 0.01, calculated as the mean land fraction along each trajectory. This excludes trajectories strongly affected by land–atmosphere interactions. We further ensure spatial relevance by applying a poleward deviation filter: trajectories must remain on or equatorward of their starting latitude, preventing inclusion of cases that deviate from the trade wind flow, where midlatitude influences could dominate cloud evolution. Additionally, an equatorward latitude shift of at least 10° is required to capture significant meridional advection consistent with the trade wind-driven tropical cloud transition. Trajectories are also required to exhibit westward longitudinal motion of at least 5°, in line with typical large-scale flow in tropical and subtropical ocean basins.

To reduce noise and avoid highly variable changes in environments, we limit SST variability by selecting only trajectories with a standard deviation in SST below 4.0 K. This constraint helps preserve trajectories within a relatively stable increase in SST with progression towards the tropics, as expected from the tropical cloud transition. It is important to note that we do not restrict cases in which the SST decreases locally, to allow for temperature gradients caused, for example, by oceanic eddies. Together, these constraints isolate a subset of trajectories suitable for analyzing ACI across evolving tropical cloud regimes. Under this framework, all remaining trajectories exhibit upward vertical velocity and precipitate at some point along their evolution, thus representing deep convection formation at a certain time in the trajectory.

The impact that each filter has on the number of retained trajectories appears in Table S1, SI. After applying these filters, the retained trajectories numbered 760 for NEP1, 1092 for NEP2, 851 for NEP3, 1080 for SEP1, 1075 for SEP2, 1603 for SEP3, 1055 for SEA1, 871 for SEA2, and 1111 for SEA3. Across all locations, the mean number of retained trajectories is 1055±242. i.e., on average, about 58% of the data passes the filtering procedure.

2.1.4 Data Grouping

To assess the influence of aerosol loading on cloud development, we divide the valid trajectories into two groups based on aerosol optical depth (AOD), using total aerosol extinction as a proxy for CCN. Here, AOD is taken from MERRA-2 reanalysis rather than directly from MODIS. MERRA-2 assimilates MODIS and AERONET observations into its global model, providing a continuous aerosol field along each trajectory and avoiding the clear-sky retrieval limitations of MODIS. For each trajectory i, AOD values are extracted across all time steps, forming a time series $A_i(t)$. We then compute the mean AOD across all N trajectories for each time step (presented in Fig. S1 SI),

$$\overline{A}(t) = \frac{1}{N}\sum_{i=1}^{N} A_i(t). \tag{1}$$

https://doi.org/10.5194/egusphere-2025-6481
Preprint. Discussion started: 5 January 2026

At every time step t, we then calculate the deviation of each trajectory from the ensemble mean, $(A_i(t) - \overline{A}(t))$. These time-resolved deviations are subsequently summed over the full trajectory length to obtain a single scalar value, which we define here as *signed deviation*:

$$D_i = \sum_{t=1}^{T} \left(A_i(t) - \overline{A}(t)\right), \tag{2}$$

which represents the cumulative difference between the trajectory's AOD and the time-dependent ensemble mean (Fig. 2). A positive D_i indicates that trajectory i tends to experience higher than average AOD levels relative to the time-evolving mean of the ensemble, while a negative D_i reflects lower than average AOD exposure. Thus, this metric captures relative aerosol loading in a way that accounts for the temporal evolution of AOD along the trajectories.

For each initiation location's dataset, we compute the median of the signed deviation values, D_{median}, and divide the trajectories into two AOD-based groups: those with $D_i \leq D_{\text{median}}$ (the clean group) and those with $D_i > D_{\text{median}}$ (the polluted group). This method ensures an approximately even split of trajectories while preserving physical meaning by classifying them based on their relative aerosol exposure, without imposing arbitrary thresholds (the mean AOD over time is shown in Fig. S1, SI). The subsequent analyses are conducted separately for the two AOD groups, within each initiation point.

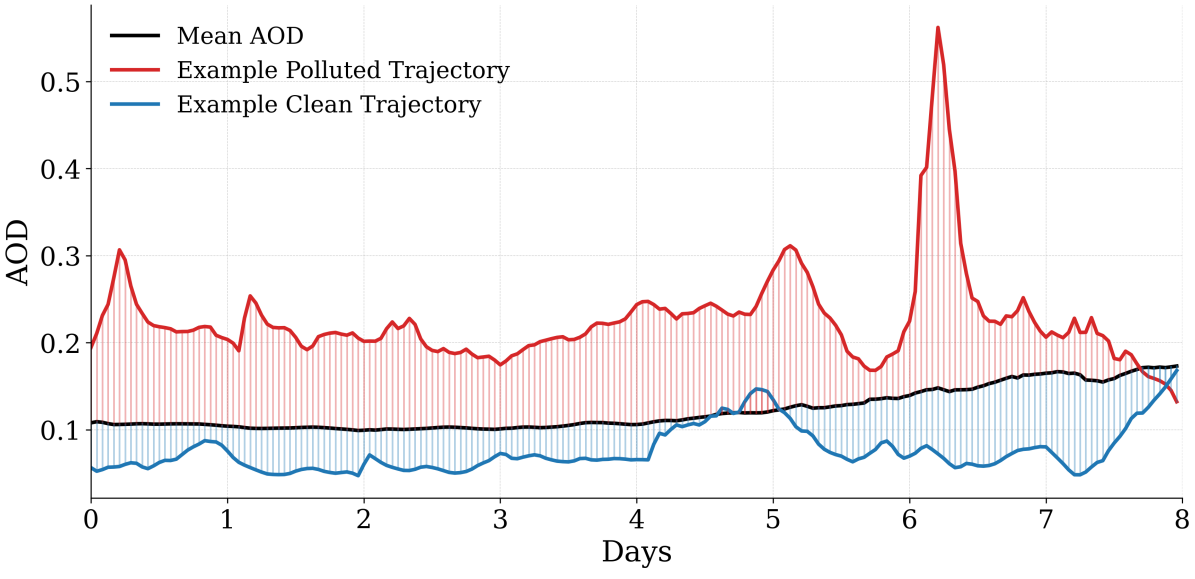

Figure 2. Time series of aerosol optical depth (AOD) for two example trajectories (from NEP1 basin), one was assigned to the polluted group (red, i = 90; 1 Apr 2019) and one assigned to the clean group (blue, i = 48; 18 Feb 2019), compared with the mean AOD across all trajectories (black). Vertical colored lines represent the signed deviation from the mean used in the trajectory classification.

https://doi.org/10.5194/egusphere-2025-6481
Preprint. Discussion started: 5 January 2026

2.1.5 MODIS Cloud Retrieval Processing

MODIS cloud properties were obtained from the collection 6.1 product for Terra (MOD06_L2) and Aqua (MYD06_L2) satellites (Platnick et al., 2016) and are collocated to the trajectories. For all liquid cloud retrievals (cloud fraction, effective radius, and liquid water path), we retain only daytime observations with solar zenith angle $< 60°$ and sensor zenith angle $< 40°$ (to avoid pixel-swelling caused by the bow-tie effect). For cloud-top height, only the sensor-zenith filter is applied since the cloud properties retrieval using the thermal channels are not affected by solar zenith angle. After screening, the hourly trajectory data are aggregated to daily means by averaging all valid retrievals across trajectories within each group (clean and polluted) for each day along the 8-day evolution. This daily-mean representation is used throughout all figures.

2.2 Numerical Simulations

The Large-Eddy Simulation (LES) model SAM (System for Atmospheric Modeling; Khairoutdinov and Randall (2003)) is used for the simulations due to its widespread application in ACI research and its ability to provide a high-resolution depiction of cloud processes. To address the impact of aerosols on tropical cloud transition, simulations are conducted using a Lagrangian framework (Sandu et al., 2010; McGibbon and Bretherton, 2017; Goren et al., 2019; Erfani et al., 2025), based on the mean trajectory derived from each initiation point in the observational data. In doing so, we do not aim to exactly reproduce the observed mean evolution, acknowledging the nonlinear relationship between individual trajectory behavior and their ensemble-mean response. The model simulates the emerging cloud evolution under two vertically uniform CCN levels of 800 cm^{-3} and 20 cm^{-3}, assuming a supersaturation of 1%. This wide range of aerosol conditions is useful for establishing physical understanding and is not intended to mimic the observed difference. The simulations use a two-moment bulk microphysics scheme (Morrison et al., 2005) and the RRTM radiation scheme (Mlawer et al., 1997). It is important to note that the aerosols are not prognostic in our simulations.

The domain size is chosen to be 57.6 $\times$ 57.6 km with 147 stretched vertical levels extending up to 33 km. Vertical grid spacing is finer (tens of meters) in the lower atmosphere to better resolve boundary-layer processes and gradually increases with height. Horizontal grid spacing is 200 m $\times$ 200 m. We use a time step of 2 seconds and a radiation time step of 30 seconds. This configuration balances the need for a sufficiently large spatial domain to resolve mesoscale cloud structures and dynamics while still resolving small-scale cloud processes at LES resolution, enabling us to capture the full tropical cloud transition (Seifert and Heus, 2013; Jansson et al., 2023). We apply small temperature perturbations ($\mathcal{O}(0.02$ K)) near the surface at the beginning of the simulation to initiate boundary-layer turbulence and allow initialization of convection. To ensure cloud presence at the start of the simulations, we initialized the model with a supersaturation of 1% linearly at the cloudy layer between the surface and the midpoint of the cloudy layer (approximately between 1000-930 hPa) during the first hour of the simulation. This step is not intended as a physical representation of supersaturation but as a practical initialization procedure to produce early cloud development consistent with the observed conditions along the Lagrangian trajectories.

https://doi.org/10.5194/egusphere-2025-6481
Preprint. Discussion started: 5 January 2026

2.2.1 Model Initial Conditions and Large-Scale Forcing

To simulate the cloud evolution along the mean trajectory, the model is configured using preprocessed, trajectory-mean observational data. This data provides surface and atmospheric properties, as well as large-scale forcing conditions. The variables are derived from the observation datasets and processed to align with the SAM input format. The model is initialized and forced using a combination of surface conditions, atmospheric profiles, and large-scale dynamical parameters. Surface forcing includes SST, sensible and latent heat fluxes, and surface momentum flux, with the latter prescribed as a constant value of 0.0784 m^2 s^{-2}, following Siebesma et al. (2003). Atmospheric initial conditions are based on vertical profiles of pressure, potential temperature, specific humidity, and horizontal wind components (zonal and meridional).

To impose realistic large-scale forcing, vertical velocity was derived from the observed pressure velocity (ω) using the relation

$$w = -\frac{\omega}{\rho \cdot g}, \tag{3}$$

where ρ is the air density (kg m^{-3}) and g is the gravitational acceleration (9.81 m s^{-2}). Additionally, large-scale wind forcing is represented by prescribing the observed zonal (u) and meridional (v) wind components. No nudging is applied to the dynamic or thermodynamic variables to allow them to evolve based on the local conditions (including the aerosol conditions).

2.3 Isolating the SST impact on q_v from the observations

To estimate water–vapor mixing ratios q_v in a way that accounts for temperature differences between polluted and clean groups, we first compute saturation quantities. The saturation vapor pressure over liquid water ($e_s(T)$) is given by

$$e_s(T) = 611.2 \exp\left[\frac{17.67\,(T - 273.15)}{T - 35.85}\right], \tag{4}$$

according to (Bolton, 1980, Eq. (10)), where T is the air temperature. The corresponding saturation mixing ratio ($q_s(T,p)$) is given by:

$$q_s(T,p) = \frac{\varepsilon\, e_s(T)}{p - (1-\varepsilon)\, e_s(T)}, \quad \varepsilon = 0.622, \tag{5}$$

where p is the air pressure. For the polluted group, we include a uniform offset, ΔT, based on the location's SST difference, to represent the observed warmer temperature background.

The reconstructed water vapor mixing ratio for each trajectory is obtained as,

$$q_v^{(grp)}(z,n,t) = \mathrm{RH}^{(grp)}(z,n,t)\; q_s\left(T_{\mathrm{ref}}^{(grp)}(z,t), p^{(grp)}(z,n,t)\right), \tag{6}$$

where the relative humidity (RH) is used in fractional form and the result is expressed in g kg^{-1}. Here, *grp* denotes the trajectory group (clean or polluted). This approach isolates the role of relative humidity from that of temperature: polluted–clean differences can thus be attributed either to the background temperature (via ΔT) or to humidity anomalies independent of temperature.

AI tools were used to assist with language editing solely for improving phrasing and clarity.

https://doi.org/10.5194/egusphere-2025-6481
Preprint. Discussion started: 5 January 2026

3 Results

3.1 Satellite Data Analysis

We start by analyzing the observational dataset to identify patterns in the evolution of polluted and clean cloud regimes. Specifically, Figures 3 and 4 show the evolution of key environmental, cloud, and radiation properties along the NEP1 dataset (starting from 34.0°N, 125.0°W) for the clean (blue) and polluted (red) groups, as an example. Equivalent figures for all other initiation points are provided in the Supplementary Information (Figs. S2-S17, SI), which exhibit generally consistent behavior across locations. Differences will be mentioned.

Across both polluted and clean groups, the trajectories reflect a gradual warming of the SST (Fig. 3a), indicative of movement from the cooler subtropics toward the warmer tropics. Simultaneously, a steady decline in lower tropospheric stability (LTS; defined as the difference in potential temperature between the 700 hPa level and the surface; Figure 3b) suggests a destabilizing boundary layer environment. Specific humidity at 850 hPa (q_v) increases markedly along the trajectories (Fig. 3c), indicating moistening of the lower free troposphere and a shift toward conditions favoring deeper convection. These thermodynamic trends are consistent with a progressive deepening of the cloud layer, as evidenced by the increasing cloud top height (CTH; Fig. 4d). Before considering aerosol differences, we note that these mean trajectories reflect the canonical tropical cloud transition.

The evolution of cloud fraction (CF; Fig. 4c) also reflects the gradual transition between cloud regimes. Initially, CF is increasing rapidly during the first day, representing the formation of extensive Sc decks during days 2-3, then declines as these decks break up into scattered Cu during days 4-5. Finally, as deep convective clouds develop in the last three days near the deep tropics, CF increases again.

As the air mass advects equatorward, liquid water path (LWP) increases during the shallow-to-deep transition, and radiative properties respond accordingly. Specifically, as the air mass moves equatorward, the TOA emitted longwave (LW) radiation decreases steadily, reflecting the rise of cloud tops into higher and thus colder layers of the troposphere. The reflected TOA shortwave (SW) radiation is initially high (during mid-day), then declines and increases back again as deep convective systems form later in the trajectory, following generally the pattern of CF. This baseline progression provides the physical context for interpreting the differences between the clean and polluted groups.

Having established the baseline tropical cloud transition, we now examine how aerosol loading modifies this evolution by comparing the clean and polluted groups. The polluted group exhibits generally smaller cloud droplet effective radii (r_e; Fig. 4a) compared to the clean group from the second day forward, consistent with the expected microphysical signature of the Twomey effect (Twomey, 1977). This reduction in droplet size coincides with a persistent enhancement in LWP (Fig. 4b) for polluted trajectories, especially during the last few days. The average LWP difference along the entire 8 days is 9.3 g m^{-2}.

Total CF (Figure 4c) is generally higher in the polluted group around the third day and onward, indicating more extensive cloud cover in the later phases of the cloud transition. This is accompanied by a faster and more pronounced increase in CTH (Fig. 4d), with polluted trajectories reaching higher cloud tops earlier in the transition and ending with deeper convection than the clean group, with a mean difference of about 1.3 km over time.

https://doi.org/10.5194/egusphere-2025-6481
Preprint. Discussion started: 5 January 2026

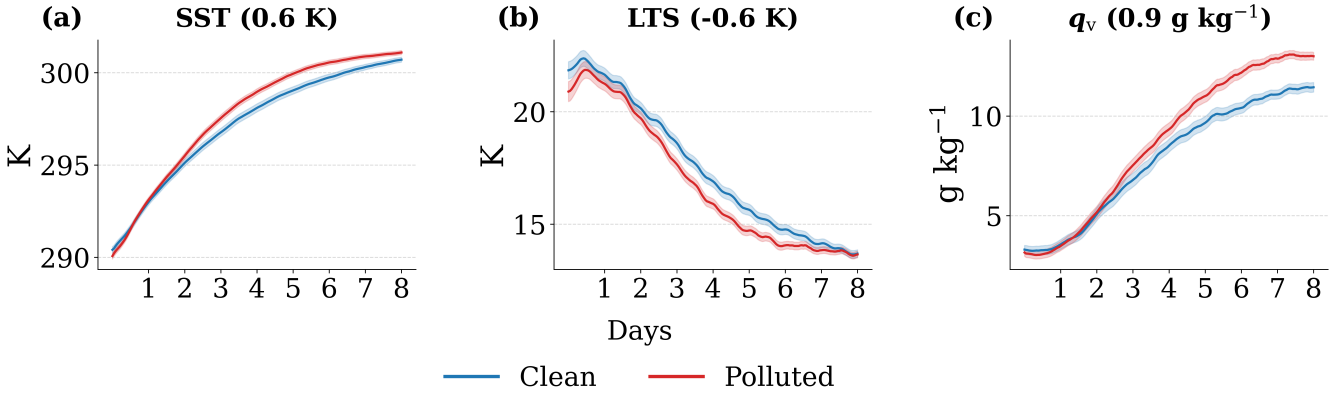

Figure 3. Hourly mean evolution of environmental variables from MERRA-2 reanalysis data along Lagrangian trajectories for the NEP1 initial location (starting from 34.0°N, 125.0°W), separated into clean (blue) and polluted (red) groups. Shown are: (a) sea surface temperature (SST), (b) lower-tropospheric stability (LTS), and (c) specific humidity at 850 hPa (q_v 850 hPa). Solid lines represent group means, shaded regions represent two-sided 95% confidence intervals for the mean, computed as mean $\pm 1.96 \times$ SEM (standard error of the mean) across trajectories at each hour. The time-mean differences between the polluted and clean trajectories are shown in parentheses above each panel.

In terms of the radiative effects in the different groups, the polluted group shows enhanced reflected TOA SW radiation (Fig. 4e) compared to the clean group, consistent with increased cloud optical thickness from smaller droplets (manifested by the decrease in r_e), higher LWP, and CF. This difference in reflected SW radiation is pronounced in the latter half of the trajectory and has a time-average difference of about 19 W m^{-2}. The emitted TOA LW radiation (Fig. 4f) is lower in the polluted group, especially in the later stages of the trajectory, with a time-mean difference of about -14 W m^{-2}, reflecting the combined influence of higher and colder cloud tops, and increased CF. These trends are consistent across all different initiation locations (Figs. S10-S17, SI; see also Fig. 8 below).

Figure 5 summarizes the daily mean differences between polluted and clean trajectory groups for all nine initiation locations, providing an observational perspective on the robustness of aerosol-related cloud adjustments. Across all basins (NEP, SEP, and SEA), a generally consistent signal emerges: polluted trajectories tend to have smaller r_e (Fig. 5a; with the exception of SEP3), higher LWP from day 3 forward (Fig. 5b), larger CF (Fig. 5c), and higher CTH (Fig. 5d) compared to their clean counterparts. The reflected SW radiation at the TOA (Fig. 5e) is higher on average for polluted trajectories across all locations, reflecting the combined effect of the generally higher LWP, greater CF, and smaller droplet sizes. Correspondingly, emitted LW radiation (Fig. 5f) is lower on average in polluted cases, consistent with higher and colder cloud tops and enhanced by a larger CF. Yet these differences cannot be attributed solely to aerosol impacts, since the two groups also differ in their underlying thermodynamic environments (Fig. 3; Figs. S2-S9, SI), reflecting potential confounding factors, i.e., co-variability with meteorological state (Gryspeerdt et al., 2019).

The opposite r_e response in the first 5 days seen in SEP3 may reflect the influence of the coastal aerosol environment off northern Chile. This region frequently experiences strong offshore gradients in cloud microphysical properties (George and

https://doi.org/10.5194/egusphere-2025-6481
Preprint. Discussion started: 5 January 2026

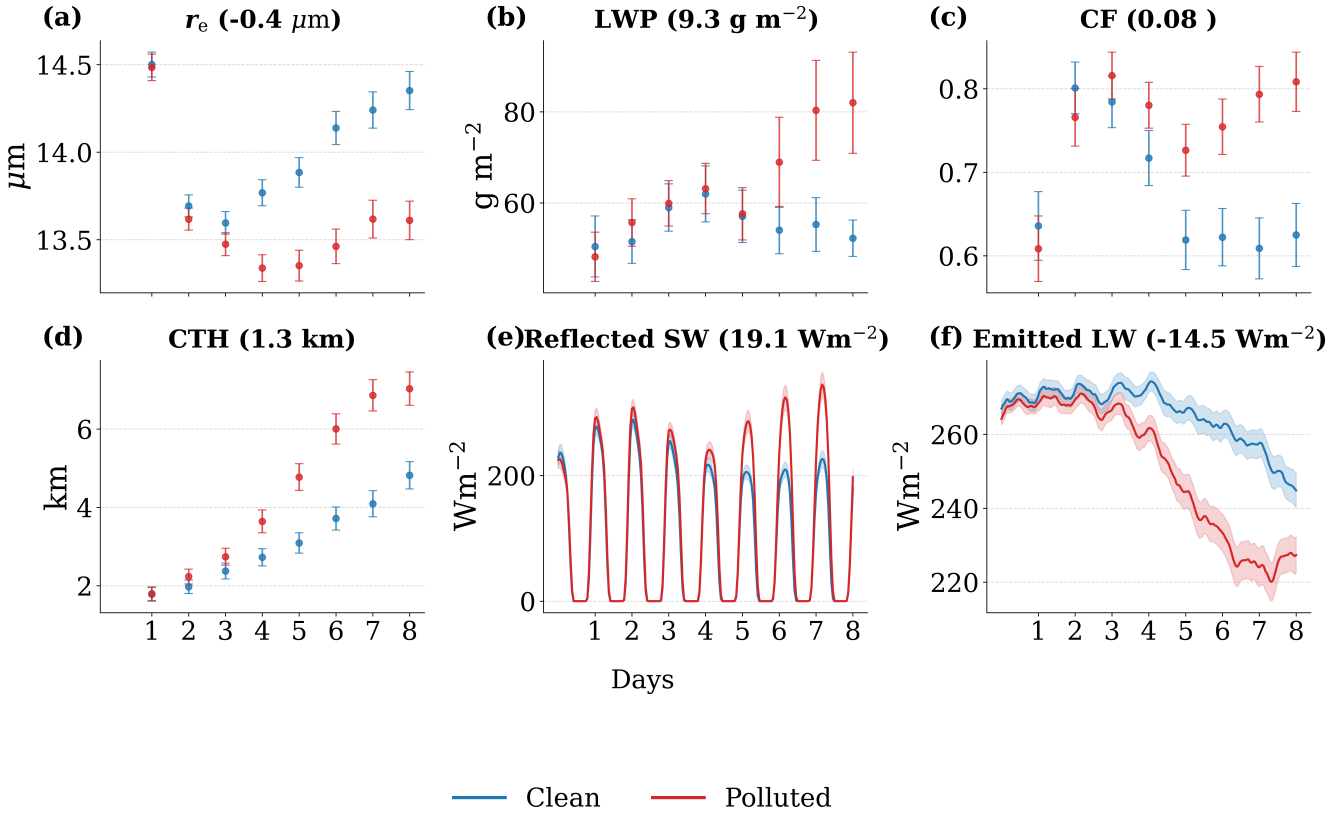

Figure 4. Mean evolution of cloud and radiation properties along Lagrangian trajectories for the NEP1 initial location (starting from 34.0°N, 125.0°W), separated into clean (blue) and polluted (red) groups. Panels (a–d) show daily means; panels (e–f) show hourly values. Shown are: (a) cloud droplet effective radius (r_e), (b) liquid water path (LWP), (c) total cloud fraction (CF), (d) cloud top height (CTH), (e) reflected shortwave radiation at Top-Of-Atmosphere (TOA; Reflected SW), and (f) emitted longwave radiation at TOA (Emitted LW). Panels a, e-f are based on CERES data, while panels b-d are based on MODIS data. Solid lines represent group means, shaded regions and error bars represent two-sided 95% confidence intervals for the mean, computed as mean $\pm 1.96 \times$ SEM (standard error of the mean) across trajectories at each point in time. The time-mean differences between the polluted and clean trajectories are shown in parentheses above each panel.

Wood, 2010; Wood et al., 2006) and episodic enhancements in sulfate outflow (Huneeus et al., 2006), which could shape the observed signal. Furthermore, satellite-retrieved AOD may include contributions from elevated aerosol layers above cloud top, which can increase column aerosol optical depth without directly affecting in-cloud microphysical processes, potentially weakening the observed cloud response (Stier, 2016; McCoy et al., 2018).

The co-variability between aerosol concentration and meteorological conditions is demonstrated in Figure 3, which presents the evolution of large-scale environmental conditions along the clean and polluted NEP1 trajectories, as an example. While both groups follow similar overall trends fitting with the tropical cloud transition- warming SST (Fig. 3a), declining lower-

https://doi.org/10.5194/egusphere-2025-6481
Preprint. Discussion started: 5 January 2026

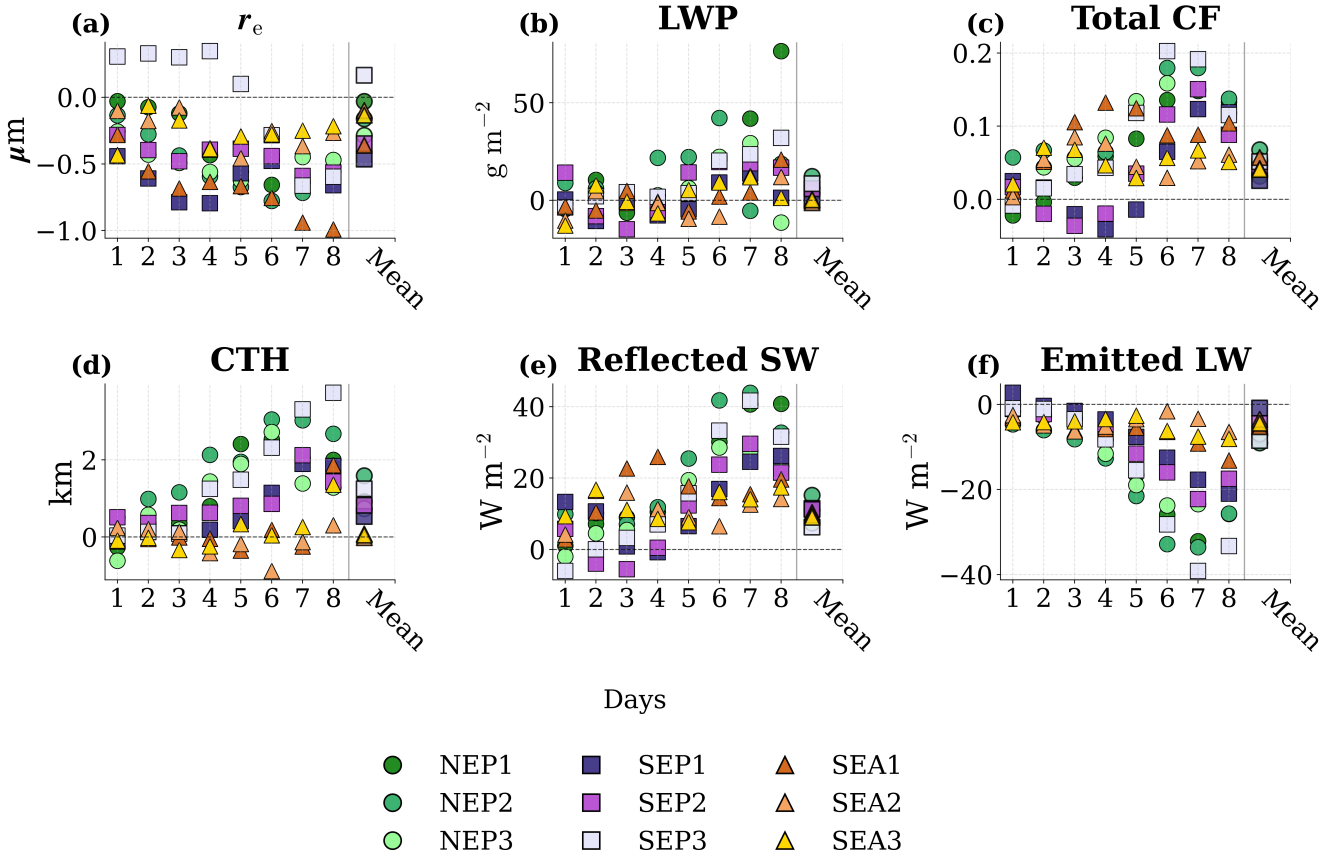

Figure 5. Daily mean differences between polluted and clean trajectory groups for all nine initiation locations (NEP1-3, SEP1-3, and SEA1-3) based on observational data. Panels show: (a) cloud droplet effective radius (r_e), (b) liquid water path (LWP), (c) total cloud fraction (CF), (d) cloud top height (CTH), (e) reflected shortwave radiation at top of atmosphere (TOA; Reflected SW), and (f) emitted longwave radiation at TOA (Emitted LW). Marker shapes and colors indicate the location, with dots representing NEP, squares representing SEP, and triangles representing SEA. The markers in the "Mean" column at the right of each panel represent the time-mean difference across all days.

tropospheric stability (LTS; Fig. 3b) and increasing q_v at 850 hPa (Fig. 3c), a systematic offset emerges between the polluted and clean groups.

Specifically, polluted trajectories exhibit slightly warmer SSTs, particularly during the mid to late stages of the cloud evolution, potentially providing a more favorable thermodynamic environment for deep convection. LTS decreases more sharply for polluted cases, implying a deepening of the inversion layer and with that, an earlier onset of deep cloud growth. q_v at 850 hPa is generally higher in the polluted group, indicating a moistening of the lower free troposphere that could enhance and sustain deep convection. These environmental differences suggest that at least part of the cloud development differences between polluted and clean trajectories (Fig. 4) may be supported or explained by variations in the environmental thermody-

https://doi.org/10.5194/egusphere-2025-6481
Preprint. Discussion started: 5 January 2026

namic conditions. The combination of higher SSTs, reduced stability, and increased lower-tropospheric moisture in polluted trajectories creates a background state more conducive to rapid cloud deepening and larger radiative impacts.

These environmental differences between clean and polluted conditions (Fig. 3) are robust across the NEP locations (Figs. S2-S9, SI), while the SEP locations show even bigger differences, with polluted trajectories consistently warmer, less stable, and moister (Figs. S4-S6, SI). In contrast, the SEA locations display the opposite behavior: polluted trajectories experience slightly cooler SSTs, and more stable and drier conditions than the clean group (Figs. S7-S9, SI), which could be driven by seasonal biomass burning from the African coast (Haywood et al. (2021); Figs. S33-35, SI). Notably, despite the opposite thermodynamic differences between clean and polluted conditions in the SEA region compared with the other basins, we still find a similar cloud and radiative response. Specifically, polluted conditions are characterized by smaller r_e, higher LWP, CF, and CTH, more reflected TOA SW radiation, and reduced TOA LW emission, as in the other basins (Fig.5). The fact that the correlation between aerosol concentration and thermodynamic conditions differs between regions, yet the pattern of the polluted–clean differences in cloud and radiation properties remains consistent, suggests that these signals cannot be fully explained by environmental variability alone.

Importantly, we also find that the two groups differ in the seasonal composition (Figs. S18-S26, SI), reflected in the number of trajectories originating from each season. These differences are indicative both of the inherent seasonality of aerosol loading in the full dataset and additional imbalances introduced by our filtering process (Sect. 2.1.3), which in turn manifests as differences in incoming solar radiation between the two groups. These seasonal differences could partly explain the observed environmental differences, even though the spatial advection paths of the trajectories remain broadly similar across seasons (Figs. S27-S35, SI). To test whether the differences between polluted and clean groups could arise from seasonality differences, we conduct sensitivity analyses using a seasonality-controlled bootstrap. The polluted-clean differences persist even after accounting for the seasonality (Fig. S61, SI).

The robustness of the sign of the differences in cloud and radiative properties between clean and polluted conditions across diverse meteorological regimes and ocean basins, which also have different seasonality (Fig. 5), supports the interpretation that the cloud microphysical and macrophysical responses to pollution: smaller droplets, enhanced LWP, CF, and deeper clouds are robust features in our satellite record.

Using AOD as a proxy for aerosol loading has known issues (Stier, 2016; Ahn et al., 2021). Hence, sulfate aerosol mass concentration (SO_4) at the 910 hPa level was also tested as an alternative proxy for aerosol loading (as was suggested in McCoy et al. (2018); Wall et al. (2022)). Both aerosol proxies (AOD and SO_4) yield generally similar cloud adjustments between polluted and clean trajectories as reported above (smaller droplet sizes, higher liquid water path and cloud fraction, and deeper clouds for polluted trajectories). However, using AOD as an aerosol proxy produces more pronounced differences in cloud-top height and radiative properties across the different locations (Fig. S60, SI). The main discrepancies between the two methods arose in the correlation between aerosols and environmental variables: for SO_4, the polluted group shows lower SST, higher lower-tropospheric stability, and lower specific humidity—opposite to the AOD-based grouping (Fig. 3). Despite these environmental differences, both aerosol proxies led to consistent cloud adjustments, suggesting that the signal is generally robust to the choice of aerosol metric.

https://doi.org/10.5194/egusphere-2025-6481
Preprint. Discussion started: 5 January 2026

3.2 Numerical Simulations

To better isolate and understand the direct influence of aerosols on cloud and radiative properties, we turn to model simulations where, by construction, the aerosol influence is decoupled from the confounding meteorological factors present in the satellite data. Unlike the observations, where aerosol and meteorological effects are intertwined, the model simulations isolate the impact of aerosols by holding environmental conditions the same between polluted and clean runs. This allows the simulated cloud adjustments to be more directly attributed to aerosol perturbations.

Figure 6 shows Hovmöller diagrams of CF from the NEP1 model simulations under clean and polluted conditions (details in sect. 3.2), presented here as an example. These diagrams illustrate the simulated evolution of cloud cover, showing the transition from Sc clouds to deep convection. At the early stages, clouds are mostly confined to the boundary layer, where shallow Sc clouds dominate below $\sim$1 km, with high CF. With time, around day 2 to 4, moistening of the lower free troposphere and gradual destabilization of the boundary layer support the breakup of Sc into scattered shallow Cu with lower CF and slightly deeper clouds, marking the transition to a more convective regime. As the lower troposphere becomes increasingly humidified, convection deepens, and cloud tops rise steadily into the mid- and upper troposphere. During the last two days of the simulation, the domain is characterized by deep convective clouds, extending above 12 km. This progression is consistent with the canonical subtropical to tropical cloud transition.

The polluted simulation (Fig. 6a) exhibits higher CF through much of the column, particularly in the mid to upper troposphere during the later stages of the trajectory. The clean simulation (Fig. 6b) also shows cloud deepening, but with reduced vertical extent and lower mid-tropospheric coverage. Figure 6c highlights these differences, with positive anomalies (red) dominating above the boundary layer in polluted cases, indicating earlier and more pronounced vertical development. This is especially pronounced during the first two days of the cloud evolution. The earlier onset of mid-level cloudiness in the polluted group suggests a faster erosion of the capping inversion and enhanced detrainment aloft, consistent with the microphysical suppression of precipitation and associated increases in LWP and CF (Fig. 7; Albrecht (1989); Bretherton et al. (2007); Stevens and Feingold (2009); Erfani et al. (2022)).

Figure 7 shows the corresponding hourly evolution of cloud and radiation variables from the model for the same simulations presented in Figure 6. The simulations reproduce the main observed trends: increasing LWP during the deepening of convection, decreasing CF during the Sc breakup, and recovering with the onset of deeper convection, and CTH rising as cloud systems grow deeper. These cloud changes with time are accompanied by radiative changes, including enhanced mid-day reflected SW and reduced emitted LW as cloud tops ascend into colder levels. While some differences in magnitude and timing exist compared to observations, the model captures the essential progression of tropical cloud transition. The time evolution of the simulations from the different initial locations is presented in Figures S44-S51, SI, and demonstrates a generally consistent behavior.

The simulated aerosol impact reproduces many of the observational signals: higher LWP—especially in the latter half of the simulation (Fig. 7b), largely similar CF (Fig. 7c), and slightly higher CTH (Fig. 7d) in polluted conditions compared to clean trajectories. The radiative responses in the model also align with the observed cloud adjustments, with polluted trajectories

https://doi.org/10.5194/egusphere-2025-6481
Preprint. Discussion started: 5 January 2026

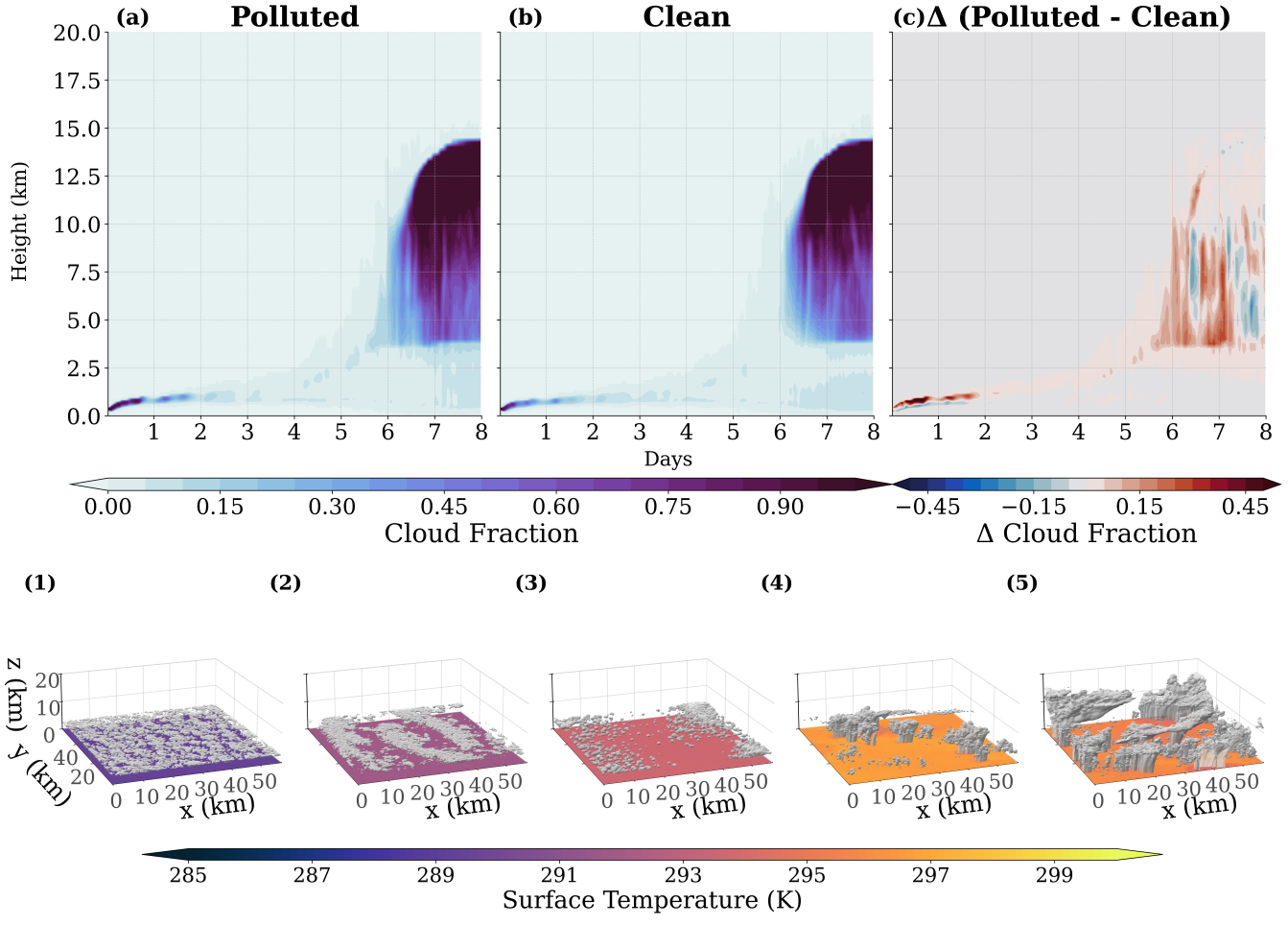

Figure 6. Hovmöller diagrams of cloud fraction evolution from model simulations for the NEP1 initial location, for the different simulated cases: (a) polluted simulation, (b) clean simulation, and (c) the difference between them (polluted − clean). Panels (a) and (b) show cloud fraction as a function of height and time, while panel (c) shows the corresponding difference field, with red indicating higher cloud fraction in the polluted case and blue indicating higher cloud fraction in the clean case. Color scales are shown below each set of panels. The bottom row (1–5) shows 3D cloud fields at selected timesteps corresponding to markers in panel (a), illustrating the temporal evolution of cloud structure from early development to mature convection. Color scales for cloud fraction and surface temperature are shown alongside each plot. The rest of the initial locations are presented in Figures S35-S42, SI.

showing enhanced reflected SW (Fig. 7e) and slightly reduced emitted LW (Fig. 7f), which is amplified by the vertical cloud deepening (Fig. 6) and the increased high-altitude cloud cover. Together, these are indicative of optically thicker clouds with higher and colder tops, consistent with the observed trend (Fig. 4). As expected, we can also see a large enhancement in N_d (Fig. 7a), which reflects the imposed increase in CCN in the domain.

https://doi.org/10.5194/egusphere-2025-6481
Preprint. Discussion started: 5 January 2026

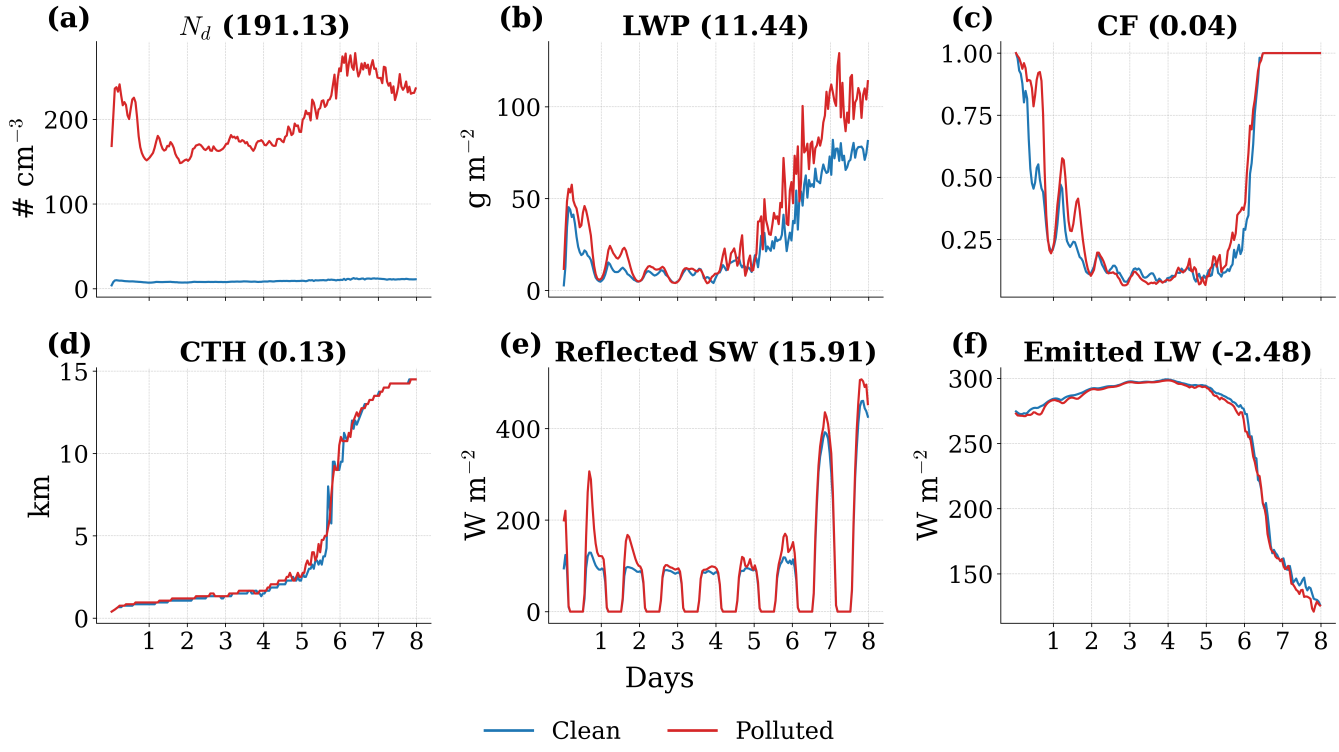

Figure 7. Hourly mean evolution of cloud and radiation variables from the model simulations for the NEP1 initial location as an example, separated into clean (blue, 20 cm^{-3}) and polluted (red, 800 cm^{-3}) simulations. Panels show: (a) Domain mean cloud droplet number concentration (N_d), (b) liquid water path (LWP), (c) total cloud fraction (CF), (d) cloud top height (CTH), (e) reflected shortwave radiation at Top-Of-Atmosphere (TOA) (Reflected SW), and (f) emitted longwave radiation at TOA (Emitted LW). The time-mean differences between the polluted and clean simulations are shown in parentheses above each panel.

To assess whether the cloud property and radiative adjustments demonstrated for NEP1 are consistent across simulated regions, we examine model-simulated polluted–clean differences for all nine initiation locations (Fig. 8). Across all basins, the model produces a coherent signal: polluted trajectories exhibit substantially higher N_d (Fig. 8a), reflecting the imposed CCN in the domain, which propagates into enhanced LWP (Fig. 8b), larger total CF (Fig. 8c), and higher CTH (Fig. 8d). These cloud adjustments highlight the systematic influence of increased aerosol concentrations on both the horizontal and vertical extent of cloud systems. Radiative responses are similarly consistent across basins. Reflected SW at the TOA (Fig. 8e) is higher on average for polluted trajectories in all locations, consistent with optically thicker and more extensive clouds. Conversely, emitted LW at TOA (Fig. 8f) is on average lower under polluted conditions, in line with higher and colder cloud tops. The magnitudes of these differences are generally comparable to those derived from the satellite observations (Fig. 5). However, the observation–model comparison is not straightforward due to the different aerosol perturbations, with model aerosol differences larger than the observed differences.

https://doi.org/10.5194/egusphere-2025-6481
Preprint. Discussion started: 5 January 2026

The consistency in both the sign and the general magnitude of these simulated responses across the NE Pacific, SE Pacific, and SE Atlantic is interpreted here as the cloud and radiation changes are robust outcomes of aerosol perturbations during marine subtropical to tropical cloud transitions.

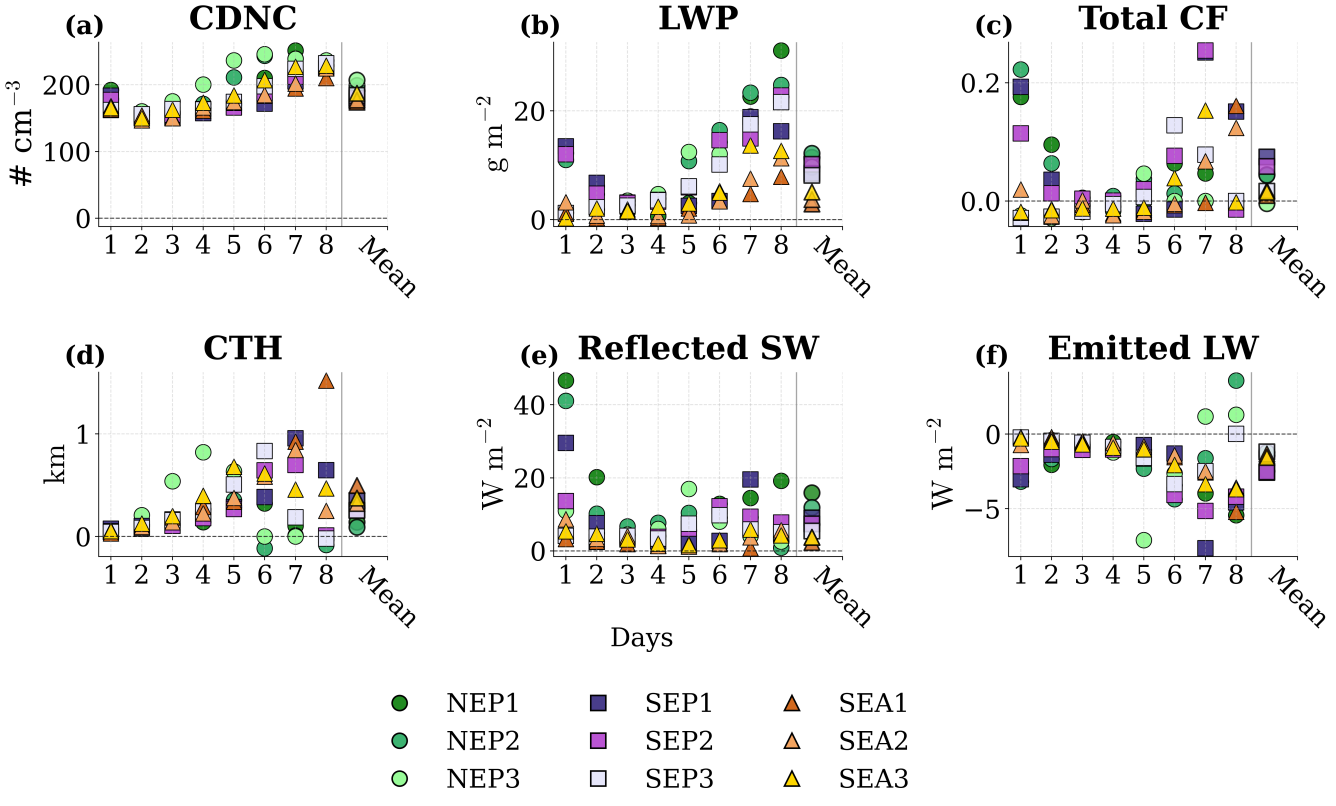

Figure 8. Daily mean differences between polluted and clean trajectory groups for all nine initiation locations (NEP1–NEP3, SEP1–SEP3, SEA1–SEA3) from model simulations. Panels show: (a) Domain mean cloud droplet number concentration (N_d) (b) liquid water path (LWP), (c) total cloud fraction (CF), (d) cloud top height (CTH), (e) reflected shortwave radiation at TOA (Reflected SW), and (f) emitted longwave radiation at TOA (Emitted LW). Marker shapes and colors indicate the location: circles (NEP), squares (SEP), and triangles (SEA). The "Mean" column indicate the time-mean difference across all days.

3.3 Aerosol–Environment Feedbacks

The interpretation of ACI from observations is complicated due to the co-variability between aerosol concentration and meteorological conditions. Air masses differ not only in aerosol loading but also in their thermodynamic environments (e.g., temperature, stability, humidity), making it difficult to determine whether observed cloud differences arise from aerosols or from pre-existing environmental variability (Gryspeerdt et al., 2016, 2019; McCoy et al., 2020; Christensen et al., 2021; Fons et al., 2023). Consequently, it is often assumed that the apparent cloud adjustments are strongly shaped, or even dominated,

https://doi.org/10.5194/egusphere-2025-6481
Preprint. Discussion started: 5 January 2026

by background meteorological variability rather than the correlated aerosol influence itself (Nishant and Sherwood, 2017; Christensen et al., 2021; Wall et al., 2022; Gulistan et al., 2024).

Here, we argue that while it is well established that aerosol–meteorology co-variability can strongly influence apparent cloud responses, an additional aspect, previously discussed in the literature (Stevens and Feingold, 2009; Lee et al., 2012; Seifert and Heus, 2013; Dagan et al., 2016), deserves further attention. Environmental changes are not only an external confounder that co-varies with aerosol loading; they can also partly arise as a consequence of aerosol–impact on clouds. Previous studies have shown that aerosols can modify cloud microphysics and vertical development in ways that subsequently feed back onto the surrounding atmospheric structure (Stevens and Feingold, 2009; Seifert and Heus, 2013; Dagan et al., 2016; Spill et al., 2019; Douglas and L'Ecuyer, 2020; Abbott and Cronin, 2021; Spill et al., 2021). According to this interpretation, differences in thermodynamic structure for different aerosol conditions arise from the combined influence of large-scale meteorological variability and aerosol-induced cloud adjustments that reshape humidity, stability, and energy transport. Thus, the environment is not only a background influence on clouds, but it can also be shaped by cloud responses to aerosols. Aerosols, therefore, act as an internal driver that shapes cloud and moisture adjustments alongside the external modulation imposed by the large-scale environment.

Figure 9 demonstrates this point by showing vertical profiles of the differences in specific humidity (q_v) between polluted and clean conditions from both observations and model simulations. Figure 9a presents the q_v profiles after accounting for SST differences between polluted and clean trajectories. Thus, they represent the humidity change, which is decoupled from the SST changes (Sect. 2.3). In the observational record (Fig. 9a), polluted trajectories show enhanced moistening near the top of the boundary layer and into the lower free troposphere. This vertical structure is consistent with cloud deepening and detrainment of moisture aloft.

The model generally reproduces this vertical structure (Fig. 9b): a moistening near and above the boundary layer top, though with a smaller magnitude and a slight drying near the surface. The general agreement between observations and model simulations (where, by design, the aerosol impact is isolated from natural co-variability with meteorological conditions) strengthens the interpretation that aerosols actively shape the thermodynamic environment through internal feedbacks, in addition to its natural co-variability.

4 Conclusions

Using five years of satellite observations combined with a trajectory model, we identified consistent differences in the evolution of cloud and radiative properties between trajectories evolving under relatively high and low aerosol loading across the Sc–Cu–DC transition, between nine distinct trajectory initiation regions spanning three ocean basins. Specifically, polluted trajectories were characterized by generally smaller r_e (mean difference of -0.2 ± 0.1 μm across the nine different initial locations, where $\pm$ indicates the 95% confidence interval of the inter-location mean), higher LWP ($4.0 \pm 3.6\ \mathrm{g\,m^{-2}}$), larger CF ($0.05 \pm 0.01$) and greater CTH ($0.7 \pm 0.4$ km) across the cloud transition. These micro and macro physical cloud adjustments were accompanied by stronger reflected SW fluxes ($10.2 \pm 2.0\ \mathrm{W\,m^{-2}}$) and reduced emitted LW fluxes ($-5.6 \pm 2.0\ \mathrm{W\,m^{-2}}$;

https://doi.org/10.5194/egusphere-2025-6481
Preprint. Discussion started: 5 January 2026

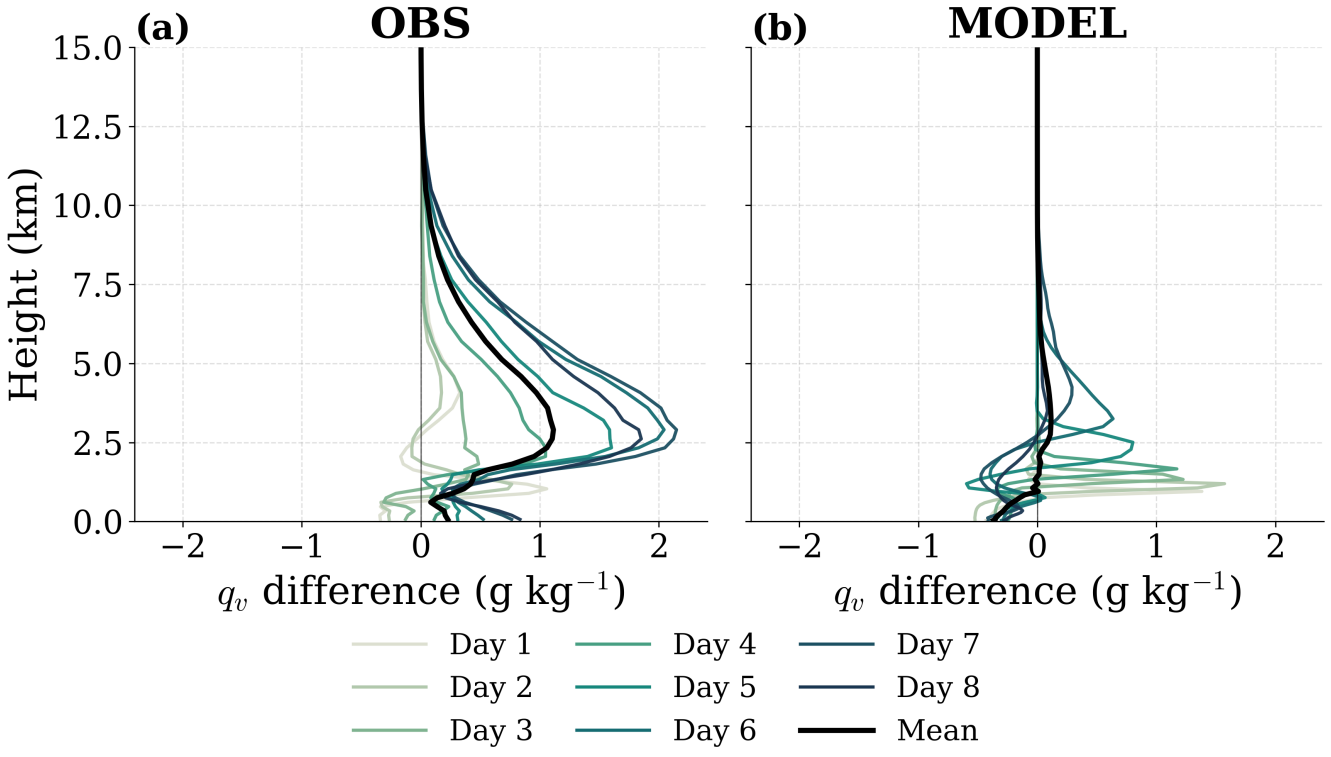

Figure 9. The difference in the vertical profile of specific humidity (q_v) between polluted and clean conditions from observations and model simulations at NEP1, as an example (the rest of the initial locations are presented in Figs. S52-S59, SI). Panel (a) shows the observed daily and time-mean differences (decoupled from the SST changes, see sect. 2.3), while panel (b) shows the corresponding model results.

Fig. 5) at the TOA. Environmental conditions also differed between the groups, with location-specific differences: polluted trajectories were generally warmer, less stable, and moister in the NEP and SEP regions, whereas the SEA region displayed the opposite tendency. Thus, model simulations were used to better isolate the aerosol-forced response from potential meteorological confounders. Model simulations confirmed the observed trends by isolating the aerosol-forced response: polluted runs with higher LWP (8.0 ± 2.6 g m^{-2}), CF (0.03 ± 0.02), and CTH (0.3 ± 0.1 km), as well as more reflected SW radiation (7.4 ± 3.3 W m^{-2}) and less emitted LW radiation (-1.8 ± 0.5 W m^{-2}) as observed in the satellite record (Fig. 8).

The consistency of differences between polluted and clean groups across all initiation locations, despite the diversity of their meteorological conditions, and the agreement with the model results, highlight aerosols as a key factor in shaping cloud evolution along the subtropical to tropical cloud transition. The robustness of our results from both approaches (Sect. 3.1 and 3.2) is reinforced by the agreement across basins spanning both hemispheres, covering various longitudinal and latitudinal ranges, representing distinct seasonal regimes, and aerosol background (Fig. S61, SI). This consistency indicates that the aerosol imprint is not tied to a specific location, but rather might be a systematic feature of the tropical cloud transition.

https://doi.org/10.5194/egusphere-2025-6481
Preprint. Discussion started: 5 January 2026

Our results extend previous works of ACI beyond the Sc to Cu transition (Yamaguchi et al., 2015; Goren et al., 2019; Christensen et al., 2020; Chun et al., 2025) into the full subtropical to tropical cloud transition, including deep convective development in the tropics. This broader view carries important implications. Since we concluded that aerosols modulate cloud depth, moistening, and radiative properties throughout the tropical transition, their impact is not limited to local microphysical and macrophysical processes. Instead, aerosols may contribute to the transport of moisture and energy within the large-scale overturning circulation, and potentially feed back on the circulation itself (Dagan et al., 2023). This non-local perspective positions aerosols not only as modulators of cloud radiative effects, but also as key players in shaping the dynamics of the tropical atmosphere.

Several limitations should be acknowledged when interpreting our results. First, while widely employed, the use of AOD as a proxy for CCN carries inherent uncertainties (Stier, 2016; Ahn et al., 2021). Satellite retrieval errors can affect AOD values above and below clouds, and AOD is not always consistently correlated with CCN due to variations in aerosol composition, size distribution, and vertical placement relative to cloud layers. Second, meteorological co-variability remains a fundamental challenge within the dataset. Polluted and clean trajectories differ not only in AOD but also in their thermodynamic environments (e.g., SST, LTS, and humidity). Despite our efforts, a complete separation of aerosol and meteorological influences could not be achieved with the observational data, because aerosol loading co-varies with large-scale meteorological conditions. This separation was only possible in the numerical simulations. Thus, part of the observed differences between the two groups may still reflect underlying meteorological variability. However, our sensitivity analyses using a seasonality-controlled bootstrap show that cloud responses remain consistent between clean and polluted conditions despite differences in thermodynamic state between trajectories. Third, our analysis is based on 8-day Lagrangian trajectories, during which air masses can experience mixing and partial loss of their initial properties, which may alter the aerosol signal over time. However, because our dataset is made up of 5 years of daily trajectories, we expect the effect to be largely averaged out and unlikely to alter the primary patterns we identify. Nevertheless, this temporal evolution represents an inherent limitation of our observational framework. In addition, our model simulations rely on idealized setups with prescribed CCN perturbations and a limited domain size. For example, our domain size is not sufficiently large to capture convective organization in the deep convective regime (Muller and Held, 2012).

Despite these limitations, the consistent aerosol signal across three ocean basins and nine initiation locations suggests that aerosol perturbations systematically amplify cloud radiative effects during subtropical to tropical transitions. This highlights how aerosols contribute to modulating tropical cloud transition and, in turn, Earth's energy budget. More broadly, our findings suggest that assessments of aerosol–cloud–climate interactions must account not only for local adjustments in cloud microphysics and macrophysics, but also for the non-local and integrated effects of aerosols across cloud regime transitions. This perspective highlights the importance of accounting for the overarching effects that aerosols may have on the large-scale circulation in both research and climate estimations.

https://doi.org/10.5194/egusphere-2025-6481
Preprint. Discussion started: 5 January 2026

Code and data availability. SAM is publicly available at: http://rossby.msrc.sunysb.edu/ marat/SAM.html The data presented in this study is publicly available at: https://doi.org/10.5281/zenodo.18031100

Author contributions. NY carried out the simulations and analyses presented. GD assisted with the simulations. NY designed and interpreted the analyses with contributions from all co-authors. NY prepared the manuscript with contributions from all co-authors. MC created the trajectories and observations dataset used here.

Competing interests. At least one of the (co-)authors is a member of the editorial board of Atmospheric Chemistry and Physics.

Acknowledgements. This research has been supported by the German Research Foundation (DFG) under grant HO 6588/3-1.

https://doi.org/10.5194/egusphere-2025-6481
Preprint. Discussion started: 5 January 2026

References

Abbott, T. H. and Cronin, T. W.: Aerosol invigoration of atmospheric convection through increases in humidity, Science, 371, 83–85, 2021.

Ackerman, A. S., Kirkpatrick, M. P., Stevens, B., and Toon, O. B.: The impact of humidity above stratiform clouds on indirect aerosol climate forcing, Nature, 432, 1014–1017, https://doi.org/10.1038/nature03174, 2004.

Ahn, S. H., Yoon, Y. J., Choi, T. J., Lee, J. Y., Kim, Y. P., Lee, B. Y., and Jung, C. H.: Relationship between cloud condensation nuclei (CCN) concentration and aerosol optical depth in the Arctic region, Atmospheric Environment, 267, 118 748, https://doi.org/10.1016/j.atmosenv.2021.118748, 2021.

Albrecht, B. A.: Aerosols, cloud microphysics, and fractional cloudiness, Science, 245, 1227–1230, 1989.

Bellouin, N., Quaas, J., Gryspeerdt, E., Kinne, S., Stier, P., Watson-Parris, D., Boucher, O., Carslaw, K. S., Christensen, M., Daniau, A.-L., et al.: Bounding global aerosol radiative forcing of climate change, Reviews of Geophysics, 58, e2019RG000 660, https://doi.org/10.1029/2019RG000660, 2020.

Bolton, D.: The computation of equivalent potential temperature, Monthly Weather Review, 108, 1046–1053, https://doi.org/10.1175/1520-0493(1980)108<1046:TCOEPT>2.0.CO;2, 1980.

Bony, S., Stevens, B., Frierson, D. M., Jakob, C., Kageyama, M., Pincus, R., Shepherd, T. G., Sherwood, S. C., Siebesma, A. P., Sobel, A. H., et al.: Clouds, circulation and climate sensitivity, Nature Geoscience, 8, 261–268, 2015.

Bretherton, C., Blossey, P. N., and Uchida, J.: Cloud droplet sedimentation, entrainment efficiency, and subtropical stratocumulus albedo, Geophysical research letters, 34, 2007.

Christensen, M., Gettelman, A., Cermak, J., Dagan, G., Diamond, M., Douglas, A., Feingold, G., et al.: Opportunistic experiments to constrain aerosol effective radiative forcing, Atmospheric Chemistry and Physics Discussions, 2021, 1–60, 2021.

Christensen, M. W., Chen, Y.-C., and Stephens, G. L.: Aerosol indirect effect dictated by liquid clouds, Journal of Geophysical Research: Atmospheres, 121, 14–636, 2016.

Christensen, M. W., Jones, W. K., and Stier, P.: Aerosols enhance cloud lifetime and brightness along the stratus-to-cumulus transition, Proceedings of the National Academy of Sciences, 117, 17 591–17 598, 2020.

Christensen, M. W., Ma, P.-L., Wu, P., Varble, A. C., Mülmenstädt, J., and Fast, J. D.: Evaluation of aerosol–cloud interactions in E3SM using a Lagrangian framework, Atmospheric Chemistry and Physics, 23, 2789–2812, 2023.

Chun, J. Y., Wood, R., Blossey, P. N., and Doherty, S. J.: Impact on the stratocumulus-to-cumulus transition of the interaction of cloud microphysics and macrophysics with large-scale circulation, Atmospheric Chemistry and Physics, 25, 5251–5271, https://doi.org/10.5194/acp-25-5251-2025, 2025.

Dagan, G.: Sub-Tropical Aerosols Enhance Tropical Cloudiness—A Remote Aerosol-Cloud Lifetime Effect, Journal of Advances in Modeling Earth Systems, 14, e2022MS003 368, https://doi.org/10.1029/2022MS003368, 2022.

Dagan, G. and Chemke, R.: The effect of subtropical aerosol loading on equatorial precipitation, Geophysical research letters, 43, 11–048, 2016.

Dagan, G. and Stier, P.: Ensemble daily simulations for elucidating cloud–aerosol interactions under a large spread of realistic environmental conditions, Atmospheric Chemistry and Physics, 20, 6291–6303, 2020.

Dagan, G., Koren, I., Altaratz, O., and Heiblum, R. H.: Aerosol effect on the evolution of the thermodynamic properties of warm convective cloud fields, Scientific reports, 6, 1–8, 2016.

https://doi.org/10.5194/egusphere-2025-6481
Preprint. Discussion started: 5 January 2026

Dagan, G., Koren, I., Altaratz, O., and Heiblum, R. H.: Time-dependent, non-monotonic response of warm convective cloud fields to changes in aerosol loading, Atmospheric Chemistry and Physics, 17, 7435–7444, 2017.

Dagan, G., Yeheskel, N., and Williams, A. I.: Radiative forcing from aerosol–cloud interactions enhanced by large-scale circulation adjustments, Nature Geoscience, 16, 1092–1098, https://doi.org/10.1038/s41561-023-01234-x, 2023.

Doelling, D. R., Sun, M., Nguyen, L. T., Nordeen, M. L., Haney, C. O., Keyes, D. F., and Mlynczak, P. E.: Advances in geostationary-derived longwave fluxes for the CERES synoptic (SYN1deg) product, Journal of Atmospheric and Oceanic Technology, 33, 503–521, https://doi.org/10.1175/JTECH-D-15-0147.1, 2016.

Douglas, A. and L'Ecuyer, T.: Quantifying cloud adjustments and the radiative forcing due to aerosol–cloud interactions in satellite observations of warm marine clouds, Atmospheric Chemistry and Physics, 20, 6225–6241, https://doi.org/10.5194/acp-20-6225-2020, 2020.

Emanuel, K. A., David Neelin, J., and Bretherton, C. S.: On large-scale circulations in convecting atmospheres, Quarterly Journal of the Royal Meteorological Society, 120, 1111–1143, 1994.

Erfani, E., Blossey, P., Wood, R., Mohrmann, J., Doherty, S. J., Wyant, M., and O, K.-T.: Simulating aerosol lifecycle impacts on the subtropical stratocumulus-to-cumulus transition using large-eddy simulations, Journal of Geophysical Research: Atmospheres, 127, e2022JD037 258, 2022.

Erfani, E., Wood, R., Blossey, P., Doherty, S. J., and Eastman, R.: Building a comprehensive library of observed Lagrangian trajectories for testing modeled cloud evolution, aerosol–cloud interactions, and marine cloud brightening, Atmospheric Chemistry and Physics, 25, 8743–8768, https://doi.org/10.5194/acp-25-8743-2025, 2025.

Fons, E., Runge, J., Neubauer, D., and Lohmann, U.: Stratocumulus adjustments to aerosol perturbations disentangled with a causal approach, npj Climate and Atmospheric Science, 6, 130, https://doi.org/10.1038/s41612-023-00435-6, 2023.

Gelaro, R., McCarty, W., Suárez, M. J., et al.: The Modern-Era Retrospective Analysis for Research and Applications, Version 2 (MERRA-2), Journal of Climate, 30, 5419–5454, https://doi.org/10.1175/JCLI-D-16-0758.1, 2017.

George, R. C. and Wood, R.: Subseasonal variability of low cloud radiative properties over the southeast Pacific Ocean, Atmospheric Chemistry and Physics, 10, 4047–4063, https://doi.org/10.5194/acp-10-4047-2010, 2010.

Glassmeier, F., Hoffmann, F., Johnson, J. S., Yamaguchi, T., Carslaw, K. S., and Feingold, G.: Aerosol-cloud-climate cooling overestimated by ship-track data, Science, 371, 485–489, 2021.

Goren, T., Kazil, J., Hoffmann, F., Yamaguchi, T., and Feingold, G.: Anthropogenic air pollution delays marine stratocumulus breakup to open cells, Geophysical Research Letters, 46, 14 135–14 144, 2019.

Goren, T., Feingold, G., Gryspeerdt, E., Kazil, J., Kretzschmar, J., Jia, H., and Quaas, J.: Projecting stratocumulus transitions on the albedo—Cloud fraction relationship reveals linearity of albedo to droplet concentrations, Geophysical Research Letters, 49, e2022GL101 169, 2022.

Gryspeerdt, E. and Stier, P.: Regime-based analysis of aerosol-cloud interactions, Geophysical Research Letters, 39, 2012.

Gryspeerdt, E., Stier, P., and Partridge, D. G.: Satellite observations of cloud regime development: the role of aerosol processes, Atmospheric Chemistry and Physics, 14, 1141–1158, https://doi.org/10.5194/acp-14-1141-2014, 2014.

Gryspeerdt, E., Quaas, J., and Bellouin, N.: Constraining the aerosol influence on cloud fraction, Journal of Geophysical Research: Atmospheres, 121, 3566–3583, https://doi.org/10.1002/2015JD023744, 2016.

Gryspeerdt, E., Goren, T., Sourdeval, O., Quaas, J., Mülmenstädt, J., Dipu, S., Unglaub, C., Gettelman, A., and Christensen, M.: Constraining the aerosol influence on cloud liquid water path, Atmospheric Chemistry and Physics, 19, 5331–5347, https://doi.org/10.5194/acp-19-5331-2019, 2019.

https://doi.org/10.5194/egusphere-2025-6481
Preprint. Discussion started: 5 January 2026

Gulistan, N., Alam, K., and Liu, Y.: Influence of covariance of aerosol and meteorology on co-located precipitating and non-precipitating clouds over the Indo-Gangetic Plain, Atmospheric Chemistry and Physics, 24, 11 333–11 349, https://doi.org/10.5194/acp-24-11333-2024, 2024.

Haywood, J. M., Abel, S. J., Barrett, P. A., Bellouin, N., Blyth, A., Bower, K. N., Coe, H., Cotterell, M. I., Davies, N. S., Dobracki, A., Fox, C., Haywood, R., Herbert, R., Johnson, B. T., Langridge, J. M., Marenco, F., McMeeking, G. R., Mulcahy, J. P., Peers, F., Taylor, J. W., Trembath, J., Wood, R., and Zuidema, P.: The CLoud–Aerosol–Radiation interaction and forcing: Year 2017 (CLARIFY-2017) measurement campaign, Atmospheric Chemistry and Physics, 21, 1049–1084, https://doi.org/10.5194/acp-21-1049-2021, 2021.

Hinkelman, L. M. and Marchand, R.: Evaluation of CERES and CloudSat Surface Radiative Fluxes Over Macquarie Island, the Southern Ocean, Earth and Space Science, 7, e2020EA001 224, https://doi.org/10.1029/2020EA001224, 2020.

Huffman, G. J., Bolvin, D. T., Nelkin, E. J., et al.: Integrated Multi-satellite Retrievals for GPM (IMERG) Version 06, Journal of Hydrometeorology, 21, 387–403, https://doi.org/10.1175/JHM-D-19-0110.1, 2020.

Huneeus, N., Gallardo, L., and Rutllant, J. A.: Offshore transport episodes of anthropogenic sulfur in northern Chile: Potential impact on the stratocumulus cloud deck, Geophysical Research Letters, 33, L19 603, https://doi.org/10.1029/2006GL027698, 2006.

Jansson, F., Janssens, M., Grönqvist, J. H., Siebesma, A. P., Glassmeier, F., Attema, J., Kölling, T., de Roode, S. R., Nuijens, L., and et al.: Cloud botany: Shallow cumulus clouds in an ensemble of idealized large-domain large-eddy simulations of the trades, Journal of Advances in Modeling Earth Systems, 15, e2023MS003 796, https://doi.org/10.1029/2023MS003796, 2023.

Kazil, J., Christensen, M. W., Abel, S. J., Yamaguchi, T., and Feingold, G.: Realism of Lagrangian large eddy simulations driven by reanalysis meteorology: Tracking a pocket of open cells under a biomass burning aerosol layer, Journal of Advances in Modeling Earth Systems, 13, e2021MS002 664, https://doi.org/10.1029/2021MS002664, 2021.

Khairoutdinov, M. F. and Randall, D. A.: Cloud resolving modeling of the ARM summer 1997 IOP: Model formulation, results, uncertainties, and sensitivities, Journal of the Atmospheric Sciences, 60, 607–625, 2003.

Lee, S. S., Feingold, G., and Chuang, P. Y.: Effect of aerosol on cloud–environment interactions in trade cumulus, Journal of the Atmospheric Sciences, 69, 3607–3632, https://doi.org/10.1175/JAS-D-11-0211.1, 2012.

Levy, R. C., Mattoo, S., Munchak, L. A., Remer, L. A., Sayer, A. M., Patadia, F., and Hsu, N. C.: The Collection 6 MODIS aerosol products over land and ocean, Atmospheric Measurement Techniques, 6, 2989–3034, https://doi.org/10.5194/amt-6-2989-2013, 2013.

Loeb, N. G., Doelling, D. R., Wang, H., Su, W., Nguyen, C., Corbett, J. G., Liang, L., Mitrescu, C., Rose, F. G., and Kato, S.: Clouds and the earth's radiant energy system (CERES) energy balanced and filled (EBAF) top-of-atmosphere (TOA) edition-4.0 data product, Journal of Climate, 31, 895–918, 2018.

McCoy, D. T., Bender, F. A. M., Grosvenor, D. P., Mohrmann, J. K., Hartmann, D. L., Wood, R., and Field, P. R.: Predicting decadal trends in cloud droplet number concentration using reanalysis and satellite data, Atmospheric Chemistry and Physics, 18, 2035–2047, https://doi.org/10.5194/acp-18-2035-2018, 2018.

McCoy, I. L., McCoy, D. T., Wood, R., Regayre, L., Watson-Parris, D., Grosvenor, D. P., Gordon, H., and et al.: The hemispheric contrast in cloud microphysical properties constrains aerosol forcing, Proceedings of the National Academy of Sciences, 117, 18 998–19 006, https://doi.org/10.1073/pnas.1922502117, 2020.

McGibbon, J. and Bretherton, C. S.: Skill of ship-following large-eddy simulations in reproducing MAGIC observations across the northeast Pacific stratocumulus to cumulus transition region, Journal of Advances in Modeling Earth Systems, 9, 810–831, 2017.

https://doi.org/10.5194/egusphere-2025-6481
Preprint. Discussion started: 5 January 2026

Mlawer, E. J., Taubman, S. J., Brown, P. D., Iacono, M. J., and Clough, S. A.: Radiative transfer for inhomogeneous atmospheres: RRTM, a validated correlated-k model for the longwave, Journal of Geophysical Research: Atmospheres, 102, 16 663–16 682, https://doi.org/10.1029/97JD00237, 1997.

Morrison, H., Curry, J., and Khvorostyanov, V.: A new double-moment microphysics parameterization for application in cloud and climate models. Part I: Description, Journal of the atmospheric sciences, 62, 1665–1677, 2005.

Muller, C. J. and Held, I. M.: Detailed investigation of the self-aggregation of convection in cloud-resolving simulations, Journal of the Atmospheric Sciences, 69, 2551–2565, 2012.

Myers, T. A. and Norris, J. R.: Observational evidence that enhanced subsidence reduces subtropical marine boundary layer cloudiness, Journal of Climate, 26, 7507–7524, https://doi.org/10.1175/JCLI-D-12-00736.1, 2013.

Neggers, R., Stevens, B., and Neelin, J.: Impact mechanisms of shallow cumulus convection on tropical climate dynamics, Journal of Climate, 20, 2623–2642, https://doi.org/10.1175/JCLI4079.1, 2007.

Nishant, N. and Sherwood, S. C.: A cloud-resolving model study of aerosol-cloud correlation in a pristine maritime environment, Geophysical Research Letters, 44, 5774–5781, 2017.

Platnick, S., Meyer, K. G., King, M. D., Wind, G., Amarasinghe, N., Marchant, B., Arnold, G. T., Zhang, Z., Hubanks, P. A., Holz, R. E., et al.: The MODIS cloud optical and microphysical products: Collection 6 updates and examples from Terra and Aqua, IEEE Transactions on Geoscience and Remote Sensing, 55, 502–525, 2016.

Quaas, J., Andrews, T., Bellouin, N., Block, K., Boucher, O., Ceppi, P., et al.: Adjustments to climate perturbations—mechanisms, implications, observational constraints, AGU Advances, 2024.

Sandu, I., Stevens, B., and Pincus, R.: On the transitions in marine boundary layer cloudiness, Atmospheric Chemistry and Physics, 10, 2377–2391, 2010.

Seifert, A. and Heus, T.: Large-eddy simulation of organized precipitating trade wind cumulus clouds, Atmospheric Chemistry and Physics, 13, 5631–5645, https://doi.org/10.5194/acp-13-5631-2013, 2013.

Siebesma, A. P., Bretherton, C. S., Brown, A., Chlond, A., Cuxart, J., Duynkerke, P. G., Jiang, H., Khairoutdinov, M., Lewellen, D., Moeng, C.-H., et al.: A large eddy simulation intercomparison study of shallow cumulus convection, Journal of the Atmospheric Sciences, 60, 1201–1219, 2003.

Spill, G., Stier, P., Field, P. R., and Dagan, G.: Effects of aerosol in simulations of realistic shallow cumulus cloud fields in a large domain, Atmospheric Chemistry and Physics, 19, 13 507–13 517, 2019.

Spill, G., Stier, P., Field, P. R., and Dagan, G.: Contrasting responses of idealised and realistic simulations of shallow cumuli to aerosol perturbations, Geophysical Research Letters, 48, e2021GL094 137, https://doi.org/10.1029/2021GL094137, 2021.

Stein, A., Draxler, R. R., Rolph, G. D., Stunder, B. J., Cohen, M., and Ngan, F.: NOAA's HYSPLIT atmospheric transport and dispersion modeling system, Bulletin of the American Meteorological Society, 96, 2059–2077, 2015a.

Stein, A. F., Draxler, R. R., Rolph, G. D., Stunder, B. J., Cohen, M. D., and Ngan, F.: NOAA's HYSPLIT atmospheric transport and dispersion modeling system, Bulletin of the American Meteorological Society, 96, 2059–2077, 2015b.

Stevens, B. and Feingold, G.: Untangling aerosol effects on clouds and precipitation in a buffered system, Nature, 461, 607–613, 2009.

Stier, P.: Limitations of passive remote sensing to constrain global cloud condensation nuclei, Atmospheric Chemistry and Physics, 16, 6595–6607, https://doi.org/10.5194/acp-16-6595-2016, 2016.

Twomey, S.: The influence of pollution on the shortwave albedo of clouds, Journal of the atmospheric sciences, 34, 1149–1152, 1977.

https://doi.org/10.5194/egusphere-2025-6481
Preprint. Discussion started: 5 January 2026

van der Dussen, J. J., de Roode, S. R., and Siebesma, A. P.: How large-scale subsidence affects stratocumulus transitions, Atmospheric Chemistry and Physics, 16, 691–701, https://doi.org/10.5194/acp-16-691-2016, 2016.

Voigt, A. and Shaw, T. A.: Circulation response to warming shaped by radiative changes of clouds and water vapour, Nature Geoscience, 8, 102–106, https://doi.org/10.1038/ngeo2345, 2015.

Voigt, A., Albern, N., Ceppi, P., Grise, K., Li, Y., and Medeiros, B.: Clouds, radiation, and atmospheric circulation in the present-day climate and under climate change, Wiley Interdisciplinary Reviews: Climate Change, 12, e694, 2021.

Wall, C. J., Norris, J. R., Possner, A., McCoy, D. T., McCoy, I. L., and Lutsko, N. J.: Assessing effective radiative forcing from aerosol–cloud interactions over the global ocean, Proceedings of the National Academy of Sciences, 119, e2210481 119, 2022.

Wang, S., Wang, Q., and Feingold, G.: Turbulence, condensation, and liquid water transport in numerically simulated nonprecipitating stratocumulus clouds, Journal of the Atmospheric Sciences, 60, 262–278, https://doi.org/10.1175/1520-0469(2003)060<0262:TCALWT>2.0.CO;2, 2003.

Wood, R.: Stratocumulus Clouds, Monthly Weather Review, 140, 2373–2423, https://doi.org/10.1175/MWR-D-11-00121.1, 2012.

Wood, R.: Assessing the potential efficacy of marine cloud brightening for cooling Earth using a simple heuristic model, Atmospheric Chemistry and Physics, 21, 14 507–14 533, 2021.

Wood, R., Bretherton, C., Huebert, B., Mechoso, C. R., and Weller, R.: VOCALS-SouthEast Pacific Regional Experiment (REx): Scientific Program Overview, Tech. rep., VOCALS Program Office, http://www.eol.ucar.edu/projects/vocals/, 2006.

Yamaguchi, T., Feingold, G., Kazil, J., and McComiskey, A.: Stratocumulus to cumulus transition in the presence of elevated smoke layers, Geophysical Research Letters, 42, 10 478–10 485, https://doi.org/10.1002/2015GL066544, 2015.

Yamaguchi, T., Feingold, G., and Kazil, J.: Stratocumulus to cumulus transition by drizzle, Journal of Advances in Modeling Earth Systems, 9, 2333–2349, 2017.